ADVANCED MATERIALS
www.advmat.de

Magneto-Ionic Engineering of Antiferromagnetically RKKY-Coupled Multilayers

Zheng Ma, Aitor Arredondo-López, Jerzy Wrona, Javier Herrero-Martín, Juergen Langer, Ocker Berthold, Eva Pellicer, Enric Menéndez, and Jordi Sort**

Voltage-driven ion motion offers a powerful means to modulate magnetism and spin phenomena in solids, a process known as magneto-ionics, which holds great promise for developing energy-efficient next-generation micro- and nano-electronic devices. Synthetic antiferromagnets (SAFs), consisting of two ferromagnetic layers coupled antiferromagnetically via a thin non-magnetic spacer, offer advantages such as enhanced thermal stability, robustness against external magnetic fields, and reduced magnetostatic interactions in magnetic tunnel junctions. Despite its technological potential, magneto-ionic control of antiferromagnetic coupling in multilayers (MLs) has only recently been explored and remains poorly understood, particularly in systems free of platinum-group metals. In this work, room-temperature voltage control of Ruderman–Kittel–Kasuya–Yosida (RKKY) interactions in Co/Ni-based SAFs is achieved. Transitions between ferrimagnetic (uncompensated) and antiferromagnetic (fully compensated) states is observed, as well as significant modulation of the RKKY bias field offset, emergence of additional switching events, and formation of skyrmion-like or pinned domain bubbles under relatively low gating voltages. These phenomena are attributed to voltage-driven oxygen migration in the MLs, as confirmed through microscopic and spectroscopic analyses. This study underscores the potential of voltage-triggered ion migration as a versatile tool for post-synthesis tuning of magnetic multilayers, with potential applications in magnetic-field sensing, energy-efficient memories and spintronics.

1. Introduction

A pressing concern facing society today is the challenge of managing the ever-increasing volumes of data, coupled with the demand for more energy-efficient data storage, transfer, and processing capabilities in next-generation micro- and nano-electronics. Memories based on magnetic materials offer several advantages over other types of memories in terms of non-volatility, density of information, writing speed, or device endurance. However, although remarkable achievements in magnetic random-access memories (MRAMs) and spintronic devices have been made utilizing spin-polarized currents to manipulate magnetism — that is, spin-transfer torque (STT) effect,[1–3] considerable electric currents are still necessary to switch the free layer (FL) in each magnetic tunnel junction (MTJ). This unavoidably leads to the Joule heating effect and high power consumption. Recently, perpendicular magnetic tunnel junctions (p-MTJs) have been proposed to reduce the current density in STT-MRAMs.[4,5] In such device architecture, perpendicular magnetic anisotropy (PMA) contributes to lowering the critical switching current compared to junctions with in-plane anisotropy. Systems with PMA also offer advantages over longitudinal configurations in realizing high areal bit densities.

At present, MTJs still face some important challenges: i) limited magnetic stability of the reference layer (RL) against external magnetic fields, ii) occurrence of interlayer dipolar interactions (i.e., the magnetic moment from the RL can interact with the FL, disturbing its magnetization reversal and degrading device performance), iii) limited thermal stability in a wide temperature range, and

Z. Ma, A. Arredondo-López, E. Pellicer, E. Menéndez, J. Sort
Departament de Física
Universitat Autònoma de Barcelona
Cerdanyola del Vallès, Barcelona 08193, Spain
E-mail: ma.zheng@uab.cat; jordi.sort@uab.cat

The ORCID identification number(s) for the author(s) of this article can be found under https://doi.org/10.1002/adma.202415393

DOI: 10.1002/adma.202415393

J. Wrona, J. Langer, O. Berthold
Singulus Technologies AG
63796 Kahl am Main, Germany

J. Herrero-Martín
ALBA Synchrotron Light Facility
Cerdanyola del Vallès, Barcelona 08290, Spain

J. Sort
Institució Catalana de Recerca i Estudis Avançats (ICREA)
Pg. Lluís Companys 23, Barcelona 08010, Spain

iv) restricted attainable areal density (i.e., scaling down the lateral size of MTJs usually compromises their performance because of superparamagnetic effects). In order to overcome these drawbacks, synthetic antiferromagnets (SAF) have been developed and used as RLs in MTJs.[6,7] SAFs essentially consist of two ferromagnetic layers antiferromagnetically coupled to each other through a non-magnetic spacer layer (e.g., Ru, Rh, or Ir) via the Ruderman–Kittel–Kasuya–Yosida (RKKY) coupling. SAFs offer enhanced magnetic robustness, reduced dipolar coupling (especially if the two ferromagnetic layers are compensated, so that no magnetic stray fields emanate from the RL), large thermal stability, more compact device design, and higher areal density. SAF structures with a more stable antiparallel alignment (i.e., larger RKKY exchange field, H_{ex}) are preferable for optimal MTJ performance since they provide a broader magnetic field range to pin the FL magnetization without unwanted interactions.

Despite the utilization of PMA and SAF structures, electric current-based magnetization switching schemes in MRAMs still pose challenges in terms of energy efficiency. Further significant reduction of ohmic loss is envisaged by using voltage (or electric fields), instead of current, to control magnetism.[8,9] Significant advances, especially in voltage control of magnetic anisotropy (VCMA) in nano-sized heterostructures, have been made in order to design and implement magnetoelectric random-access memories (MeRAMs).[10,11] For instance, by applying sub-nanosecond voltage pulses, coherent magnetization switching of the FL in MTJs can be accomplished.[12] VCMA has also been exploited to induce the switching of CoFeB FLs in p-MTJ devices by modifying the interface between the tunnel oxide barrier and the ferromagnetic layer.[13] From a more fundamental perspective, extensive studies have been performed to electrically modulate other distinct parameters, such as magnetization, magnetic anisotropy, coercivity, transition temperature, ON-OFF switching of ferromagnetism, topological states (e.g., skyrmions or domain bubbles), as well as other interfacial effects (e.g., exchange bias or, more recently, the RKKY coupling) in a variety of magnetic and spintronic materials.[14–17] Much effort has been devoted to multiferroic materials where the magnetic and electric order parameters are coupled (either in single-phase or heterostructured multiferroics). However, most conventional multiferroic candidates (e.g., $BiFeO_3$ and $TbMnO_3$) are not compatible with CMOS technology. This, together with other limitations such as the weak coupling between electric polarization and magnetization at room temperature (in single-phase multiferroics), or the clamping effects with the substrate in ferroelectric/magnetostrictive coupled bilayers, remain to be overcome to harness their full potential in realistic devices. In turn, pure electric-field effects can modulate coercivity,[18] magnetic anisotropy,[19] or Curie temperature[20] of diluted magnetic semiconductors by altering the carrier density with a gate voltage. Nevertheless, the low Curie temperature of most of these semiconductors is a serious shortcoming. Because of all these drawbacks, the use of voltage-driven ion motion to manipulate magnetism (i.e., magneto-ionics) has gained increasing interest in recent years.[16,21–23] Voltage-induced ion transport between a magneto-ionic target and an electrolyte (solid or liquid) can electrochemically alter the target's crystallographic phase and composition reversibly—changes that would otherwise be considered impossible after the material has been prepared and put into use. As a result, magneto-ionics represents a promising avenue for achieving significant, non-volatile modulation of magnetic properties. Through this approach, control of a wide range of magnetic and spin phenomena has been demonstrated in systems ranging from metals to oxides or nitrides. For instance, reversible toggling of magnetic anisotropy (between in-plane and out-of-plane directions) at room temperature has been realized by H^+ insertion/removal at a Co/GdO_x interface under gate voltage application.[24] Moreover, analogous to the brain's active fluidic ion transport and restoration, magneto-ionics allows emulating synapses with speeds down to ms or even µs, offering exciting opportunities for energy-efficient brain-inspired (neuromorphic) computing.[25–27]

From all the above reasons, it is clear that modulation of antiferromagnetically RKKY coupled multilayers (MLs) with electric field is of great interest and technological relevance for MRAM development. Yang et al. reported ionic liquid gating control of RKKY interaction in Co/Pt-based MLs,[28] where dissimilar behaviors, including hysteresis loops with one, two, or three switching steps were observed. However, the details of the magnetization reversal and the underlying mechanisms responsible for those observations remained unclear due, in part, to the complex chemical processes involved during liquid electrolyte gating. Recently, the effects of H^+,[29] Li^+[30], or O^{2-}[31] ion migration on the RKKY coupling in Co/Pd- and Co/Pt-based MLs have been also explored. These works have reported small modifications of the H_{ex} field, by tens of Oe, resulting in ferromagnetic-antiferromagnetic transitions in the RKKY interaction; yet, the evolution of microstructure and composition inside the stacks upon gating was overlooked. Additionally, important challenging aspects such as the non-volatility and long-term stability of magneto-ionic effects induced in RKKY multilayers, as well as voltage-driven transitions between ferrimagnetic (non-compensated) and antiferromagnetic (compensated) states in this kind of systems (besides the aforementioned transitions between ferromagnetic and antiferromagnetic interactions[31]) remain to be investigated in detail. The latter is of particular interest to tune the magnetic stray fields and dipolar coupling between the FL and RL comprised in the MTJs.

Another important aspect of MRAM technology is that, in order to mitigate the dependence on critical raw materials and to contribute to environmental sustainability, it is highly desirable to avoid the use of platinum-group metals (e.g., Pt, Pd) in ferromagnetic MLs, although Pt/Co or Pd/Co stacks are usually needed to achieve large PMA. In this direction, interesting results have been obtained in recent years in Ni/Co MLs, which can exhibit high spin polarization,[32,33] low intrinsic damping[32,34,35], and PMA that can be tuned by varying the sublayer thickness.[36,37] However, magneto-ionic control of magnetism in Pt- or Pd-free SAF systems has not been reported thus far.

In this work, magneto-ionic effects in Co/Ni-based SAFs with strong PMA are systematically investigated. We demonstrate large voltage control of various RKKY interaction effects in these systems, including transitions between uncompensated (ferrimagnetic) and fully compensated (antiferromagnetic) states, as well as strong modulation of the RKKY bias field offset, occurrence of additional switching events, and eventual formation of

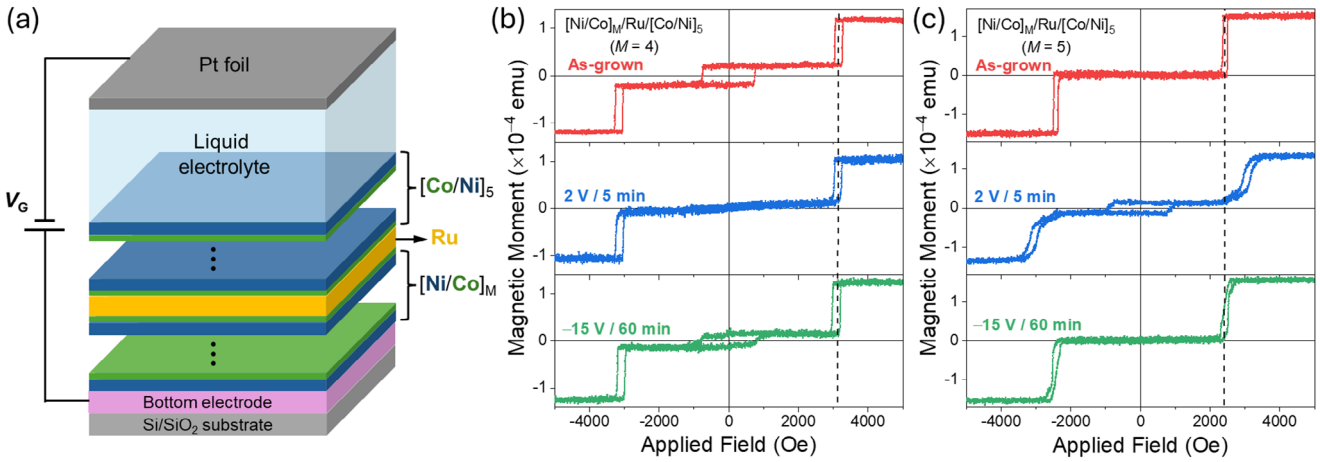

Figure 1. Voltage control of transitions between antiferromagnetic and ferrimagnetic states in perpendicularly magnetized SAF MLs. a) Schematic illustration of the composition of the ML stacks and electrolyte gating configuration. Gate voltage, V_G, is applied between the partially masked bottom electrode and a Pt foil of a similar area (counter electrode) during the gating experiments. b, c) Room-temperature hysteresis loops of the as-grown (top panels), voltage-treated (+2 V for 5 min, middle panels) and recovered (−15 V for 60 min, bottom panels) [Ni/Co]$_M$/Ru/[Co/Ni]$_5$ samples (t_{Ru} = 0.9 nm), where M = 4 and 5 for panels (b) and (c), respectively.

skyrmion-like or pinned magnetic domain bubbles. Remarkably, we achieve modifications of H_{ex} by >1000 Oe by applying a relatively low gating voltage (2 V). The observed modulation of magnetic properties is attributed to voltage-controlled oxygen ion motion in the MLs, as corroborated by transmission electron microscopy (TEM) and energy dispersive X-ray spectroscopy (EDX) observations, together with X-ray absorption (XAS) and magnetic dichroism measurements.

2. Results and Discussion

2.1. Controlling the Transition from Antiferromagnetic to Ferrimagnetic Ground States and Vice Versa

We investigated the influence of the sublayer thickness on the magnetic anisotropy in Co/Ni-based multilayers (see Figure S1, Supporting Information). A maximized PMA is found for a Co thickness of 0.25 nm and Ni thickness of 0.60 nm, in excellent agreement with previous reports.[37,38] Thus, these thicknesses were chosen for designing [Ni/Co]$_M$/Ru/[Co/Ni]$_5$ SAF heterostructures (the subscripts M and 5 refer to the Ni/Co or Co/Ni bilayer repeats in the bottom and top MLs, respectively), as shown in **Figure 1a**. In this Section, the Ru spacer thickness is fixed to be 0.90 nm,[37] and the bottom bilayer number is M = 4 (i.e., uncompensated) or 5 (i.e., compensated), to favor macroscopic antiferromagnetic interlayer coupling with different magnetic moment compensation between the top and bottom MLs at magnetic field H = 0 Oe. The top panels of Figure 1b, c show the out-of-plane hysteresis loops of the as-grown [Ni/Co]$_4$/Ru/[Co/Ni]$_5$ and [Ni/Co]$_5$/Ru/[Co/Ni]$_5$ SAFs, respectively. While for the former, a typical four-step hysteresis loop with finite remanent magnetization is observed, the latter shows a three-step switching process with a zero net moment at H = 0 Oe, as expected. These observations can be explained by considering RKKY coupling energy, J_{ex}, which can be expressed as:

$$J_{ex} = n\left(t_{Co}M_{S,Co} + t_{Ni}M_{S,Ni}\right)H_{ex} \quad (1)$$

where n is the number of bilayer repeats, t_{Co} and t_{Ni} are the thicknesses of Co and Ni sub-layers, respectively, and $M_{S,Co,}$ and $M_{S,Ni}$ are the corresponding saturation magnetization values. Note that J_{ex} depends on t_{Ru} and remains constant for a given t_{Ru} (e.g., 0.90 nm). In the [Ni/Co]$_4$/Ru/[Co/Ni]$_5$ stacks, owing to its lower repeat number n, the bottom ferromagnetic [Ni/Co]$_4$ ML switches before the top [Co/Ni]$_5$ ML as H decreases from positive saturation. That is, the magnetization reversal of the bottom ML is essentially responsible for the high-field minor loop centered at H = 3160 Oe in this stack (see Figure 1b). At remanence, the top and bottom MLs remain antiparallel aligned but, since their number of repeats is different, a net moment is obtained at H = 0 Oe. That is, the [Ni/Co]$_4$/Ru/[Co/Ni]$_5$ sample (top panel) is a synthetic ferrimagnetic stack at remanence. This is opposite to what happens in Figure 1c, where the remanence is zero, evidencing full compensation of the antiferromagnetic order (because, in this case, the total number of repeats is the same for the top and bottom MLs, i.e., n = 5). The overall switching behavior of the synthetic ferrimagnet (e.g., Figure 1b) will be described in more detail in Section 2.

For magnetoelectric characterization, magnetic moment vs time curves were measured while applying gating voltage between the underlying electrode layer and a Pt foil across a liquid electrolyte in a closed electrochemical cell (see Experimental Section). Magnetic hysteresis loops of the gated heterostructures were recorded immediately after the applied voltage was switched off, with the sample still immersed inside the liquid electrolyte but always at 0 V. For comparison, hysteresis loops of the as-grown heterostructures were also acquired before any voltage application. Typical magnetic moment vs time curves under 2 and 10 V are shown in Figure S2 (Supporting Information). Notably, faster and more pronounced changes in the magnetic moment are observed for the SAF stack gated at higher voltage. Several important observations can be made upon the application of a positive gate voltage of 2 V for 5 min on the SAF structures. First, the saturation magnetic moment decreases upon gating for both SAFs (see the top and middle panels of

Figure 1b,c). This suggests the oxidation of the top [Co/Ni] ML due to voltage-driven diffusion of oxygen ion species from an eventual surface passivation layer and/or the liquid electrolyte, as elaborated later. The contribution of oxygen ion species from the liquid electrolyte may come from i) propene and carbonate species resulting from the cathodic decomposition of propylene carbonate during the initial voltage actuation,[39] ii) molecular O_2 dissolved in the electrolyte, and iii) hydroxyl ions produced upon electrolyte drying (see Experimental Section). But, more remarkably, because of the magneto-ionic effect, the originally uncompensated SAF (i.e., with $M = 4$ in the bottom multilayer, and 5 repeats on the top multilayer) becomes fully compensated after gating for 5 min (that is, a transition from ferrimagnetic to antiferromagnetic states is induced with voltage, as shown in Figure 1b middle panel). In contrast, for the gated $[Ni/Co]_5/Ru/[Co/Ni]_5$ structures (initially compensated), an additional minor hysteresis loop develops at low fields after gating, leading to the generation of an uncompensated moment at $H = 0$ Oe (Figure 1c middle panel). In this case, the oxidation effect reduces the net moment in the top multilayer, causing the unbalance between top and bottom magnetization values. Furthermore, reversibility tests reveal that the observed ferri-to-antiferromagnetic transition and the antiferro-to-ferrimagnetic transition can return to their initial states (uncompensated or compensated, respectively) by applying asymmetric gating of opposite polarity (i.e., −15 V), as shown in the bottom panels of Figure 1b,c. In other words, using voltage as a post-deposition technique, we achieve magnetic transitions between uncompensated (ferrimagnetic) and compensated (antiferromagnetic) states, which is of particular interest for spintronic device applications based on SAF MLs. It is also noteworthy that the two SAFs behave quite differently at the high-field ranges. For instance, while the shape and position of the minor loops are nearly unaltered for the $[Ni/Co]_4/Ru/[Co/Ni]_5$ samples (Figure 1b), in the $[Ni/Co]_5/Ru/[Co/Ni]_5$ stack, the high-field minor loops become largely tilted and shifted to higher fields upon gating (i.e., from $H = \pm 2500$ Oe for the as-grown to $H = \pm 3040$ Oe for the treated state, see Figure 1c). These observations can be understood based on the magneto-ionic effect. Namely, for the $[Ni/Co]_4/Ru/[Co/Ni]_5$ samples (Figure 1b), the minor loop corresponds to the switching of the bottom layer (which is presumably not affected by oxidation, as will be shown later), in the voltage-treated $[Ni/Co]_5/Ru/[Co/Ni]_5$ samples, the top layer switches first because the oxidation causes a reduction of the effective Co/Ni number of repetitions (see Equation 1). The tilt of the minor loop is due to a loss of PMA of the top ML, probably resulting from partial disruption of the smooth Co/Ni interfaces upon oxidation. In addition, since the top ML has now a lower magnetic moment, and assuming that J_{ex} remains constant (i.e., that the oxidation effect does not reach Ru and its thickness is kept constant), H_{ex} increases to compensate for the reduction of the $n(t_{Co}M_{S,Co}+t_{Ni}M_{S,Ni})$ term.

2.2. Magneto-Ionic Control of RKKY Effects in Synthetic Ferrimagnetic Multilayers

In this section, we focus on voltage modulation of the magnetic properties in uncompensated SAFs (or synthetic ferrimagnets) with RKKY interlayer coupling. It is well known that the RKKY interaction oscillates with the distance between the top and bottom ferromagnetic layers, i.e., the Ru thickness in this case. Thus, fabricating SAF structures with different spacer thicknesses is the most straightforward way to tune the RKKY interaction and antiferromagnetic coupling strength in SAFs.[30,40] Here, we deposited a series of $[Ni/Co]_7/Ru/[Co/Ni]_5$ SAFs with Ru thickness, t_{Ru}, ranging from 0.35 to 1.05 nm. $M = 7$ in the $[Ni/Co]_M/Ru/[Co/Ni]_5$ heterostructures was chosen to achieve a stable ferrimagnetic configuration with a strong signal. **Figure 2a,b** present schematics of the magnetic moment orientations along with representative magnetic hysteresis loops of the deposited layer stacks. Indeed, a significant influence of t_{Ru} on hysteretic behavior is found. For instance, while the moment in a $[Co/Ni]_5$ ML switches collectively as a single ferromagnet (single hysteresis loop, as shown in red in Figure 2b), a four-step spin reversal behavior is observed in $[Ni/Co]_7/Ru/[Co/Ni]_5$ for certain spacer thicknesses (e.g., $t_{Ru} = 0.40$ nm, or $0.75 \leq t_{Ru} \leq 1.05$ nm) as H is swept from positive to negative saturation. This is attributed to the RKKY interlayer coupling, which favors antiparallel alignment between the top and bottom MLs. As illustrated in the bottom panel of Figure 2a, assuming that the spins of the top and bottom ferromagnetic MLs align upward at positive saturation fields, a descending H from positive saturation would first switch the moment of the top [Co/Ni] ML from upward (step 1) to downward (step 2), owing to its smaller repeat number compared to the bottom counterpart (5 vs 7–see Equation 1). Then, when H sweeps to the negative direction and increases in magnitude, switching of the bottom [Ni/Co] ML from up to down directions occurs, which is accompanied by a back-switching of the top Co/Ni due to the antiferromagnetic RKKY interaction through the Ru (step 3). Finally, further sweeping the field toward negative saturation will realign the moment of the top ML downward (step 4). For the case of $t_{Ru} = 0.60$ and 0.70 nm (see Figure 2b), a three-step spin-switching process is observed as the H field sweeps from positive to negative saturation. In this case, the RKKY exchange energy is too weak to favor the back-switching of the top ML at negative fields; instead, the Zeeman energy is dominant and tends to readily align the moment along the H direction. Figure 2c shows the dependence of the exchange field, H_{ex}, and exchange coupling strength, J_{ex}, as a function of Ru spacer thickness. Two clear antiferromagnetic coupling minima peaks, located at $t_{Ru} = 0.40$ and 0.90 nm, are visible within the studied Ru thickness range. As t_{Ru} increases, the typical oscillatory decay behavior of the RKKY interlayer coupling is evident.

Next, magnetometry measurements were carried out on the $[Ni/Co]_7/Ru/[Co/Ni]_5$ SAFs with the maximum antiferromagnetic RKKY coupling (i.e., $t_{Ru} = 0.40$ and 0.90 nm) while in situ gating. **Figure 3a** shows the influence of gating time (under 2 V) on the hysteresis loops of the 0.90 nm stack. Figure 3c summarizes the dependences of the antiferromagnetic coupling field, H_{ex}, the total saturation moment, m_S, as well as the saturation moment (m_{S_1} and m_{S_2}) and the slopes of the loops at the critical switching fields (χ_1 and χ_2) for the low- and high-field minor loops, respectively, as indicated in the loop in Figure 3b. Similar to what was observed in Figure 1c, longer gating duration tends to shift the high-field minor loop toward higher magnetic fields (i.e., increasing H_{ex}). Meanwhile, the low-field loop gets progressively narrower and taller (i.e., m_{S_1} increases). Remarkably, the RKKY field increases from 2375 Oe for the

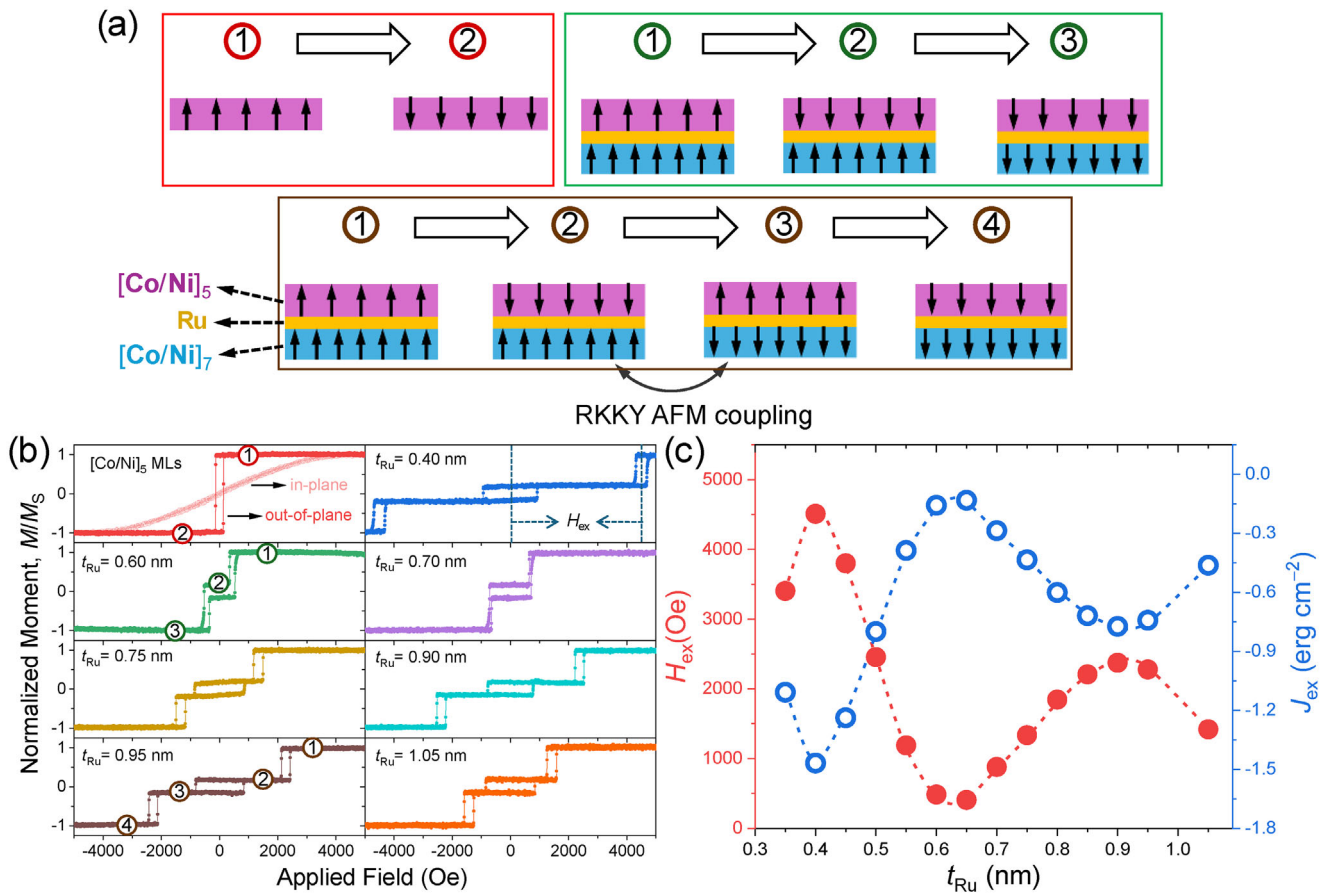

Figure 2. Magnetic hysteresis behavior of the as-grown $[Ni/Co]_7/Ru/[Co/Ni]_5$ stacks with variable Ru thickness, t_{Ru}. a) Schematics of magnetic moment reversal for the uncoupled $[Co/Ni]_5$ stacks (in red), and representative schematics of spin switching of top and bottom MLs in $[Ni/Co]_7/Ru/[Co/Ni]_5$ stacks with three- (t_{Ru} = 0.60 nm, in green) and four- (t_{Ru} = 0.95 nm, in dark brown) steps. The black arrows indicate the spins of the top and bottom ferromagnets. b) Room-temperature hysteresis loops of the as-grown $[Co/Ni]_5$ MLs and $[Ni/Co]_7/Ru/[Co/Ni]_5$ stacks with variable t_{Ru}. Applied magnetic fields are along out-of-plane direction with respect to the film plane, unless otherwise specified. c) Dependence of the RKKY coupling field, H_{ex}, and exchange coupling strength, J_{ex}, as a function of t_{Ru}.

as-grown sample to ≈3780 Oe for the sample gated under 2 V for 55 min. That is, the field range with antiferromagnetic stability gets considerably enhanced, which is particularly interesting for MRAM device implementation. As discussed before, the high-field minor loop corresponds to the magnetization reversal of the top ML. Considering that the effective thickness of this ML gets reduced due to the voltage-driven oxygen insertion (an effect that will be shown in detail in Section 3), it is expectable that H_{ex} increases based on Equation 1. The increase of m_{S_1} derives from the increase in the unbalanced moments between the top and bottom MLs (since the top ML gets oxidized while the bottom ML remains unaltered). A tradeoff of the observed H_{ex} enhancement is the gradual decrease in PMA (i.e., drops in χ_1 and χ_2). However, the sample remains largely perpendicularly magnetized, and a finite saturation m_{S_2} is noticeable even for the longest-term gated sample. This suggests the robustness of the RKKY exchange in the SAFs. Similar behaviors are observed in the 0.40 nm SAF structures. Remarkably, in this case, a considerably high H_{ex} of ≈5800 Oe is obtained after gating for 55 min, which is amongst the highest H_{ex} for this type of material in the literature.[41,42] Finally, we explored the reversibility of the observed voltage control of magnetic properties (see Figure S3, Supporting Information). Partial reversibility is found for 2 V voltage actuation, but it can be largely improved with a lower gating voltage.

To further explore magneto-ionic phenomena in SAFs, we also studied $[Ni/Co]_7/Ru/[Co/Ni]_5$ structures with other t_{Ru} values. Interestingly, as shown in **Figure 4**, for t_{Ru} = 0.60 nm, aside from the aforementioned effects (e.g., H_{ex} enhancement, loss of PMA, and increase of uncompensated moment), an additional switching event starts to develop at about $H = \pm 850$ Oe after gating for 10 min under 2 V. The appearance of the new spin switching process can be understood from an induced structural inhomogeneity in the top ML during gating (as schematically illustrated in Figure 4c). Whereas regions with thicker Co/Ni ML (less affected by O^{2-} insertion) switch similarly to the as-grown state, other regions with thinner Co/Ni could contribute to the occurrence of the additional spin-switching event at high fields. This claim is supported by high-resolution TEM (HRTEM) observations, revealing the appearance of mixed nanocrystalline/amorphous grains in the voltage-actuated sample (see Experimental Section and Figure S4, Supporting Information). It is worthwhile to

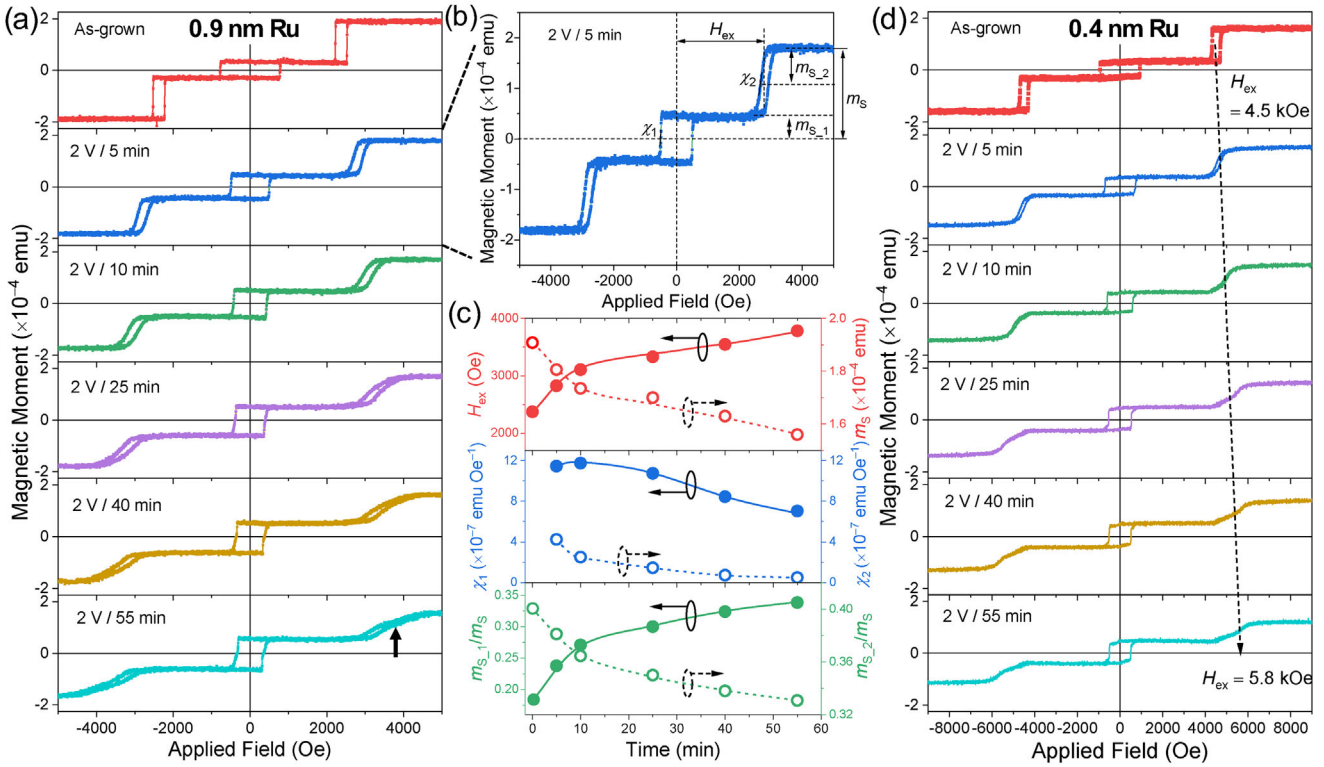

Figure 3. Voltage control of the hysteresis loops behavior of $[Ni/Co]_7/Ru/[Co/Ni]_5$ SAF stacks (t_{Ru} = 0.40 and 0.90 nm). a) Evolution of the hysteresis loops as a function of voltage actuation time for the stack with 0.90 nm thick Ru. b) A representative hysteresis loop corresponding to the 2 V/5 min treated SAF heterostructure, where the RKKY coupling field, H_{ex}, the total saturation moment, m_S, as well as the saturation moment (m_{S_1} and m_{S_2}) and the loops slopes at the switching fields (χ_1 and χ_2) are indicated for the low- and high-field loops, respectively. These parameters are quantified in c) as a function of gating time for the sample with t_{Ru} = 0.90 nm. d) Evolution of the hysteresis loops as a function of voltage actuation time for the stack with 0.40 nm thick Ru.

mention that voltage-driven non-uniform O^{2-} transport was already observed in magneto-ionically actuated CoO_x thin films.[43,44] Similar effects may also happen in our MLs. Figure 4b presents the effects of gating time on the hysteresis loops of the SAF stack with t_{Ru} = 1.05 nm. In this case, whereas the as-grown sample shows four-step magnetization switching, the loop of the final gated structures reveals the occurrence of six plateaus, as indicated in Figure 4d. Interestingly, the actuated sample (at 2 V for 55 min) has been re-measured six months after the original measurement, and the shape of the hysteresis loop remains identical, evidencing the long-term stability of the induced magneto-ionic effects (see Figure S5, Supporting Information). Finally, note that by applying the same gating protocols to the SAF with t_{Ru} = 0.75 nm, which exhibits a comparable RKKY coupling as the sample with t_{Ru} = 1.05 nm (see Figure 2c), similar dependencies and an eventual six-step magnetic moment switching upon gating are observed, as shown in Figure S6 (Supporting Information). The additional switching event is not exclusive of these two Ru thicknesses. The sample with t_{Ru} = 0.9 nm also tends to show an incipient additional step at high fields after gating for 55 min (as indicated by the upward arrow in Figure 3a). Such events are visible to a larger or smaller degree depending on the values of H_{ex} and the strength of PMA. Overall, these results reveal that voltage-driven ion motion represents a novel approach to engineering multiple magnetic states in SAFs taking advantage of magneto-ionically induced lateral inhomogeneities in the magnetic MLs, an effect that has been correlated with the eventual formation of textured ground states in these systems with potential applications in spintronics.[45] It should be noted that controlling such SAFs systems with voltage is promising in terms of energy efficiency. While STT-MRAMs typically operate with spin-polarized currents of the order of 100 μA,[46] here the measured currents are two orders of magnitude lower (thus minimizing Joule heating effects). Detailed studies have shown that in voltage-controlled magnetic memory systems (i.e., actuated through the converse magnetoelectric effect) the write energy can be as low as 10^{-3} pJ/bit, which is two orders of magnitude lower than in STT-MRAM devices.[46–48] However, further optimization is needed in magneto-ionically controlled SAFs to decrease the actuation times from several minutes to μs or lower (rates that are already attainable in some other magneto-ionic systems[49–51]).

After demonstrating the emergence of additional magneto-ionically induced magnetic states and switching events, as well as the enhancement of H_{ex} at the expense of effective PMA through voltage application, it is intriguing to illustrate the distinct evolution of magnetic domain patterns that occurs before and after voltage actuation. **Figure 5** shows the polar magneto-optic Kerr effect (MOKE) microscopy images of the $[Ni/Co]_7/Ru/[Co/Ni]_5$ SAF (t_{Ru} = 1.05 nm) after gating under 2 V for 55 min. These MOKE images were collected from a minor loop (that corresponds to the magnetization reversal of the top ML) by sweeping the field between the saturated state

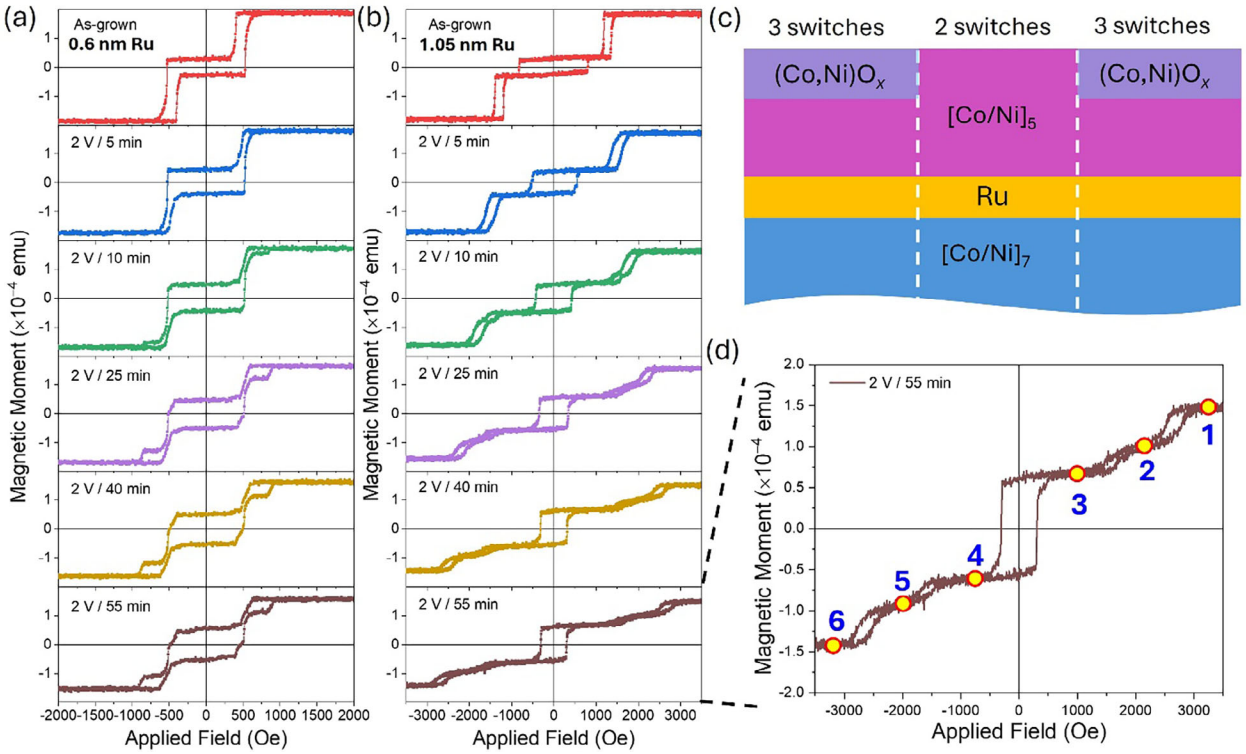

Figure 4. Voltage control of the hysteresis behavior of $[Ni/Co]_7/Ru/[Co/Ni]_5$ stacks (with t_{Ru} = 0.60 and 1.05 nm), showing the generation of additional magnetization switching events upon gating. a, b) Evolution of hysteresis loops as a function of gating time. c) Schematic representation of the formation of inhomogeneous magnetic regions in the top ML of the SAF stack with t_{Ru} = 0.60 nm, which could lead to the observed new magnetization states. d) Enlarged view of the final hysteresis loop in b), clearly showing the appearance of a six-plateau step-like loop after applying +2 V for 55 min.

and H = 500 Oe. A more general view, including the images of the whole loop for the as-grown and treated stacks, is shown in Figure S7 and Video S1 (Supporting Information). In contrast to the as-grown sample, which shows no signs of visible domain formation under our measurement conditions (due to the associated strong PMA which results in very sharp transitions at the coercive fields of each sub-loop), we observe the appearance of "skyrmion-like" or pinned magnetic domain bubbles (2–3 μm in diameter) near the minor-loops coercive fields of the gated stack, as seen in Figure 5b,c. The occurrence of domain nucleation/propagation following the gradual magnetization reversal process is accompanied by analog variations of magnetic moment (instead of sudden jumps), which may find applicability for neuromorphic applications (modulation of synaptic weight, voltage-driven synaptic plasticity, multilevel storage, etc.).[27]

Finally, while liquid gating has been utilized in this work to demonstrate magneto-ionic control of RKKY interaction effects in Co/Ni-based MLs, similar effects might be induced in the future using all-solid device configurations. This could be achieved by integrating the magneto-ionic MLs with ion-conducting polymers, ionic gels, or solid electrolytes exhibiting high ionic conductivity (e.g., Gd-doped CeO_2 or Y_2O_3-doped ZrO_2[25,52,53]). A proposed solid-state magneto-ionics-based MTJ device is illustrated in Figure S8 (Supporting Information). While liquid electrolyte gating enables the generation of large electric fields with moderate voltages via narrow electric double layers, and also prevents electric pinhole issues, transitioning to solid-state devices might be interesting for future device integration with long-term operational stability.

2.3. Structural Insights into the Magneto-Ionic Atomic Migration Mechanism

Scanning transmission electron microscopy (STEM) and energy dispersive X-ray spectroscopy (EDX) techniques were utilized to investigate the local structural and compositional characteristics. The cross-sectional STEM-EDX analyses, as well as the integrated intensity profiles, clearly reveal the distinct oxygen distributions in the top Co/Ni ML for the as-grown and voltage-actuated $[Ni/Co]_7/Ru/[Co/Ni]_5$ SAF stacks with t_{Ru} = 1.05 nm, as shown in **Figure 6**. Except from the ≈2 nm top surface (passivation layer), the oxygen distribution is uniform and its content is ≈5 at.% (see Figure 6a–c), possibly stemming from the natural oxidation of the TEM lamella. The amount of oxygen for the top ML increases with the gating time. Oxygen-rich regions are identified at the top 3–4 nm after gating under 2 V for 10 min (see Figure 6d–f), unambiguously corroborating the voltage-induced O^{2-} transport into the ML. The relative amounts of Ni and Co are concomitantly reduced, indicating the formation of mixed CoNi oxides. The enhancement of oxygen intensity is more obvious, and the effects tend to be seen at deeper depths for longer voltage actuation (Figure 6g–i) due to the progressive O^{2-} insertion into the stack with voltage. For instance, within the top 2 nm, the ratio between oxygen and metal (Co+Ni) (i.e., relative concentration) increases from ≈1.0 for the as-grown stack to 1.4 for the

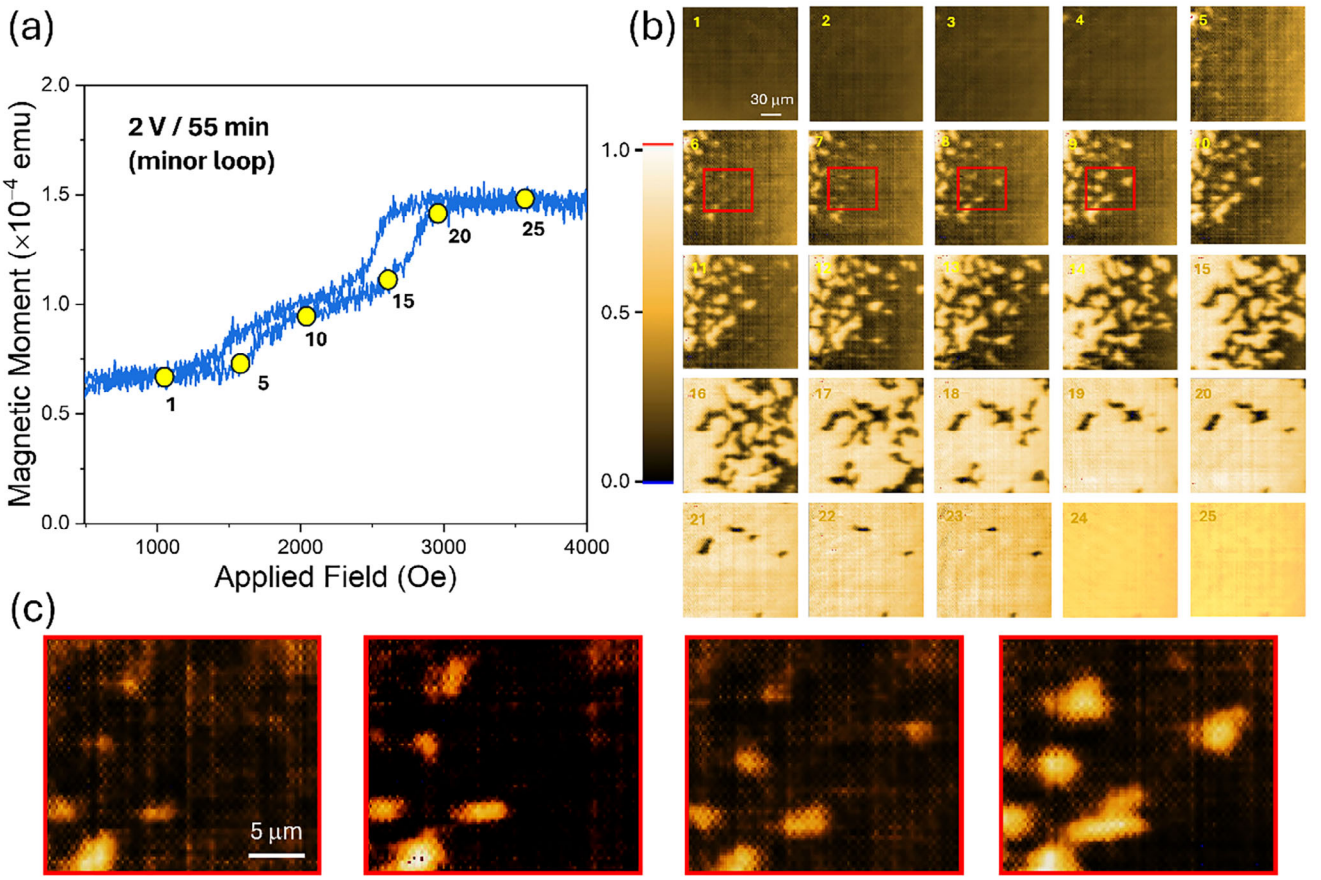

Figure 5. MOKE microscopy imaging of the voltage-treated $[Ni/Co]_7/Ru/[Co/Ni]_5$ SAF stack (with t_{Ru} = 1.05 nm), in the magnetic field range of 500–4000 Oe, showing nucleation and propagation of magnetic domains, that are otherwise not observable in the as-grown sample. a) Typical high-field minor hysteresis loop of this sample recorded by vibrating sample magnetometry (VSM), highlighting the approximate magnetic fields where the MOKE images were acquired. b) shows the occurrence of skyrmion-like or circular domain bubbles during nucleation of magnetic domains. Note the scale is normalized into the range between 0 and 1. c) Enlarged view of the regions (red rectangles) highlighted in (b).

sample gated for 55 min. Moreover, while oxygen mainly concentrates on the top 2 nm in the as-grown films, oxygen migrates approaching the Ru spacer (down to 4–5 nm) after voltage actuation for 55 min. HRTEM also shows a lowered degree of crystallinity and the formation of nanocrystalline/amorphous regions in the top MLs after voltage actuation (see Figure S4, Supporting Information), which is probably responsible for the loss of PMA and the additional switching transitions, as described in Section 2. It seems plausible to speculate that such effects may be related to the chemical composition variations due to oxygen insertion.

To probe the voltage-induced changes in electronic and magnetic structures, X-ray absorption spectroscopy (XAS) and X-ray magnetic circular dichroism (XMCD) measurements were performed under a 10 kOe out-of-plane magnetic field, at room temperature, for the as-grown $[Ni/Co]_7/Ru/[Co/Ni]_5$ SAF (with t_{Ru} = 1.05 nm) and the same sample gated for different times. **Figure** 7a,b shows the Co and Ni $L_{2,3}$-edges XAS and XMCD spectra, collected in the total electron yield mode, which enables an effective sampling depth of ≈5 nm (i.e., mainly probing the top Co/Ni layers). Characteristic XAS spectra of metallic Co and Ni are found in the pristine state,[54,55] as expected. Upon gating, the appearance of a pre-peak at ≈778 eV (denoted by the pink downward arrow in Figure 7a) is ascribed to the high-spin Co^{2+}.[54] Moreover, a shoulder becomes visible at the high-energy side of the Co L_3-edge, indicated by the cyan downward arrow in Figure 7a. This, together with the shift of the Co L_2-edge to higher energy (see the black dashed arrow in Figure 7a), clearly corroborates the gradual development of 2+ and/or 3+ Co valence states with gating. As for the Ni $L_{2,3}$-edges XAS of the treated stack, the emergence of the high-energy peak at ≈856 eV (marked by the purple downward arrow in Figure 7b) and the double-peak feature at the Ni L_2-edges indicate the existence of bivalent Ni cations.[55,56] The comparison of the XMCD spectra, as shown in the bottom panels of Figure 7a,b, unambiguously reveals that the dichroic signal for both Co and Ni $L_{2,3}$-edges is progressively suppressed upon gating. This is related to the voltage-driven electrochemical process in the top Co/Ni layers, in agreement with the TEM-EDX and XAS results, suggesting oxidation of the top ML stack when positive voltage is applied. Moreover, the XMCD spectral shapes of the gated samples remain practically identical to that of the as-grown sample (see Figure S9, Supporting Information), indicating the non-ferromagnetic nature of the newly formed species after gating, in line with the oxidation of metallic Co/Ni induced by gating.

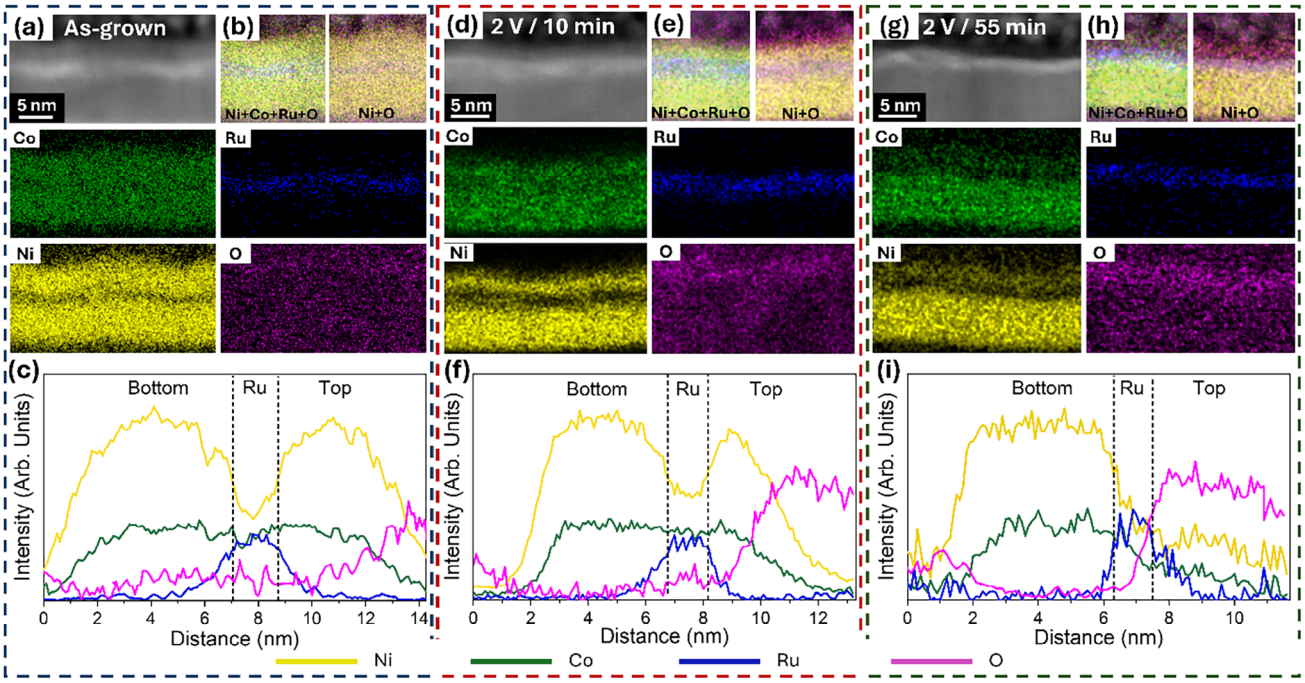

Figure 6. Structural and compositional characterizations of the as-grown and voltage-treated $[Ni/Co]_7/Ru/[Co/Ni]_5$ SAF structures (t_{Ru} = 1.05 nm). a, d, g) STEM images of the as-grown and voltage-treated (2 V/10 min and 2 V/55 min) lamellae. b, e, h) Corresponding EDX elemental mapping and chemical concentration results for both overlayed (Ni+Co+Ru+O and Ni+O) and separate Co (green), Ru (blue), Ni (yellow) and O (pink) components. c, f, i) Integrated depth profiles showing the compositional evolution for each sample. The vertical dotted lines denote the approximate boundaries between the ferromagnetic MLs and the spacer layer.

The spin (m_S) and orbital (m_L) magnetic moment, as well as the total moment, m_{TOT}, ($m_{TOT} = m_L + m_S$), are quantified from the XMCD spectra by using the corresponding sum rules,[57,58] and their evolutions are plotted in Figure 7c,d. As seen in Figure 7c, m_S, m_L, and m_{TOT} of Co undergo a concomitant monotonic decrease with gating, owing to the formation of metal oxides (e.g., CoO and/or Co_3O_4). For instance, the spin component continuously drops from m_S = 1.027 μ_B/atom for the as-grown state to 0.903 μ_B/atom for the 2 V/10 min gated sample, until reaching 0.632 μ_B/atom for the 2 V/55 min gating treatment. Similarly, a decreasing trend is observed for the magnetic moment of Ni.

3. Conclusion

In this work, unprecedented control of RKKY interaction effects in Co/Ni-based MLs through voltage-driven ion motion (magneto-ionics) is demonstrated. Reversible transitions between uncompensated (ferrimagnetic) and fully compensated (antiferromagnetic) states are achieved in these structures by changing the applied voltage polarity. If incorporated in MTJs, such transitions are of interest to tune magnetic stray fields and interlayer dipolar coupling between the free and pinned layers in MTJs. In general, the occurrence of dipolar interactions can shift the coercive field of the free layer, making it harder (or easier) to switch than intended or creating undesirable energy barriers that could lead to asymmetric switching behavior. Thus, the ability to control such dipolar interactions at will offers additional degrees of freedom to optimize the performance of MTJs. Our results also reveal strong modulation of the RKKY bias field offset (over 1000 Oe) at room temperature under a low gating voltage (2 V), increasing the magnetic-field stability range of MTJs. Such an effect is accompanied by a decrease of PMA in the top ML which, although in principle is detrimental, facilitates the formation of skyrmion-like or pinned domain-wall magnetic bubbles. Furthermore, for certain compositions, we observe the emergence of additional switching events, likely related to voltage-driven structural inhomogeneities in the gated MLs. Tuning of magnetic properties is linked to voltage-driven oxygen migration, particularly in the upper ML (i.e., magneto-ionic effects), as confirmed by scanning transmission electron microscopy, X-ray absorption spectroscopy, and magnetic circular dichroism measurements. Our findings enhance the understanding of magneto-ionic control of RKKY effects in SAF systems and highlight the potential of magneto-ionics as a powerful post-synthesis tool for engineering magnetic multilayers with novel and enhanced functionalities.

4. Experimental Section

Sample Preparation: All samples, including $[Co/Ni]_5$ MLs with variable Co and Ni sub-layer thicknesses, $[Ni/Co]_M/Ru/[Co/Ni]_5$ stacks with different repeat numbers (M = 4, 5, or 7), and Ru thickness (t_{Ru} = 0.35–1.05 nm), were deposited at room temperature on smooth CuN-based conductive seed layers, previously grown on Si/SiO_2 substrates. For the depositions, a Singulus TIMARIS ten-cathode PVD system was used, which incorporates the full scope of sputtering techniques: DC, pulsed DC, and RF magnetron sputtering as well as combinations of these modes. In this case (all metallic layers) DC sputtering was used, which was an economical solution for many types of metal coatings. Its primary limitation was that low-conducting materials tend to take on charge over time

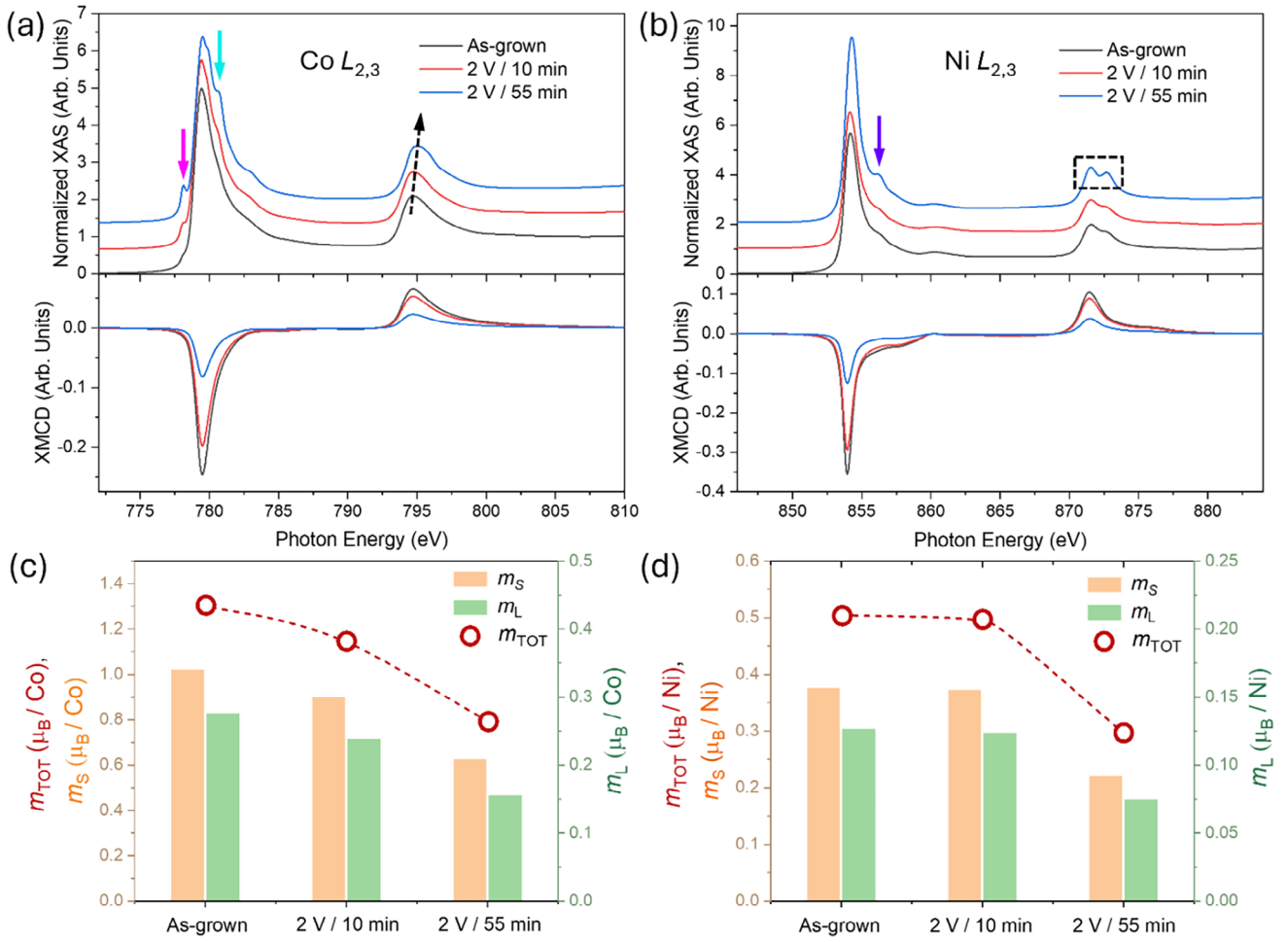

Figure 7. X-ray absorption and X-ray magnetic dichroism study of the as-grown and voltage-treated $[Ni/Co]_7/Ru/[Co/Ni]_5$ SAF (t_{Ru} = 1.05 nm). a) Co $L_{2,3}$ and b) Ni $L_{2,3}$ edges XAS and XMCD spectra for the as-grown and gated samples (under 2 V/10 min and 2 V/55 min conditions). c,d) show the dependence of the Co and Ni magnetic moments per atom obtained from applying the sum rules to the XMCD data for the three states. The total moment, m_{TOT} amounts to the sum of the spin (m_S) and orbital (m_L) moments. Note the different Y-axis scales in panels (c) and (d).

(charging issue), eventually leading to arcing, poisoning of the target material, and, as a consequence, reduced quality of deposited samples and loss of device functionality. To overcome this limitation, RF or DC pulsed sputtering could be used, although these alternative modes were not necessary in this case. Before the deposition of the SAF structures, the seed layers were partially masked to be employed as working electrodes in an electrochemical cell during magnetometry measurements under in situ voltage gating.

In Situ Magnetometry Study: Magnetometry measurements were performed using a Lakeshore 8600 series vibrating sample magnetometer (VSM) magnetometer at room temperature. For standard in situ magnetoelectric measurements, magnetic moment vs time curves were recorded while applying a gate voltage of 2 V between the working electrode and a Pt foil (acting as a counter electrode) in a liquid electrolyte, using an Agilent B2902A power supply. During the measurements, the foil was placed parallel and at 2 mm from the sample surface, in a capacitor-like configuration. Propylene carbonate with traces of dissolved Na^+ (10–25 mg L^{-1}) and OH^- ions, obtained from the reaction of metallic Na with traces of water, was used as the liquid electrolyte. Before gating under 2 V, a voltage actuation step consisting of applying −15 V to the stacks for 20 min was conducted to minimize eventual effects from surface passivation. Hysteresis loops were recorded either before (as-grown state) or immediately after (gated state) applying voltage, while the sample under study remained in the liquid electrolyte but with the voltage switched off. The applied magnetic fields were up to 9 kOe, normal to the film plane (i.e., out-of-plane direction), if not otherwise specified. A field step of 5 Oe/step and an integration time of 0.8 s were used to have an adequate signal/noise ratio. High-field linear background signals, arising from the sample holder, electrochemical cell, and substrate, were subtracted.

Magneto-Optic Kerr Imaging Study: Magneto-optic Kerr effect microscopy images of the as-grown and voltage-treated magnetic stacks were collected at ambient temperature using NanoMOKE 3 equipment from Durham Magneto Optics in polar geometry. The MOKE spot size was ≈3–5 microns, with resolution limited by the laser wavelength, making it difficult to resolve domains smaller than 1 micron. Magnetic domain imaging was performed by sweeping the magnetic field along the whole hysteresis loops, and, in more detail (small field steps), around certain transition fields.

Transmission Electron Microscopy and Energy Dispersive X-Ray Analysis: TEM and EDX spectroscopy analyses were performed at 200 kV on Spectra 300 (Thermo Fisher Scientific) monochromated STEM microscope with double aberration correction. Cross-sectional thin lamellae were prepared by focused-ion-beam (FIB) milling. Before the FIB preparation, the samples were sputter-coated with a Pt protective layer to prevent beam damage and reduce charging.

X-Ray Absorption and Magnetic Dichroism Measurements: Room-temperature XAS and XMCD measurements at the Co and Ni $L_{2,3}$ edges were carried out for the as-grown and voltage-treated SAF samples at the BOREAS beamline of the ALBA synchrotron (Barcelona, Spain).[59] The base pressure was below 10^{-7} Torr. The incident beam was 20° tilted with respect to the sample normal. An out-of-plane magnetic field of 10 kOe was applied during the measurements. Absorption spectra were recorded in a sequence of $\mu^+\mu^-\mu^-\mu^+\mu^-\mu^+\mu^+\mu^-$, where μ^+ and μ^- correspond to the respective spectra using left- and right-circularly polarized beams. The XAS and XMCD spectra were calculated as the sum and the difference, respectively, of the averaged spectra measured with the two opposite helicities.

Supporting Information

Supporting Information is available from the Wiley Online Library or from the author.

Acknowledgements

Financial support by the European Research Council (2021-ERC-Advanced REMINDS Grant No. 101054687), the Generalitat de Catalunya (2021-SGR-00651), and the Spanish Government (PID2020-116844RB-C21, PDC2021-121276-C31, TED2021-130453B-C22 and the MCIN/AEI/10.13039/501100011033 & "European Union NextGenerationEU/PRTR" grant CNS2022-135230) were acknowledged. This work was conducted within the NICKEFFECT project, funded by the European Union's Horizon Europe Research and Innovation Programme, under Grant Agreement no. 101058076. Authors acknowledged the use of instrumentation financed through Grant IU16-014206 (METCAM-FIB) to ICN2 funded by the European Union through the European Regional Development Fund (ERDF), with the support of the Ministry of Research and Universities, *Generalitat de Catalunya*. The XAS/XMCD experiments were performed at the BL29-BOREAS beamline at ALBA Synchrotron with the collaboration of ALBA staff under the in-house research proposal 2024018031. E.M. is a Serra Húnter fellow.

Conflict of Interest

The authors declare no conflict of interest.

Data Availability Statement

The data that support the findings of this study are available from the corresponding author upon reasonable request.

Keywords

magneto-ionics, perpendicular magnetic anisotropy, RKKY interactions, synthetic antiferromagnets, voltage control of magnetism

Received: October 9, 2024
Revised: March 6, 2025
Published online: March 20, 2025

[1] J. C. Slonczewski, *J. Magn. Magn. Mater.* **1996**, *159*, L1.
[2] L. Berger, *Phys. Rev. B* **1996**, *54*, 9353.
[3] A. V. Khvalkovskiy, D. Apalkov, S. Watts, R. Chepulskii, R. S. Beach, A. Ong, X. Tang, A. Driskill-Smith, W. H. Butler, P. B. Visscher, *J. Phys. D: Appl. Phys.* **2013**, *46*, 074001.
[4] S. Ikeda, K. Miura, H. Yamamoto, K. Mizunuma, H. D. Gan, M. Endo, H. Ohno, *Nat. Mater.* **2010**, *9*, 721.
[5] Y. Zhang, W. Zhao, Y. Lakys, J. O. Klein, J. V. Kim, D. Ravelosona, C. Chappert, *IEEE Trans. Electron. Dev.* **2012**, *59*, 819.
[6] S. Bandiera, R. C. Sousa, Y. Dahmane, C. Ducruet, C. Portemont, V. Baltz, S. Auffret, I. L. Prejbeanu, B. Dieny, *IEEE Magn. Lett.* **2010**, *1*, 3000204.
[7] K. Yakushiji, A. Fukushima, H. Kubota, M. Konoto, S. Yuasa, *Appl. Phys. Express* **2013**, *6*, 113006.
[8] K. L. Wang, J. G. Alzate, P. K. Amiri, *J. Phys. D: Appl. Phys.* **2013**, *46*, 074003.
[9] Y. Shiota, S. Miwa, T. Nozaki, F. Bonell, N. Mizuochi, T. Shinjo, Y. Suzuki, *Appl. Phys. Lett.* **2012**, *101*, 102406.
[10] X. Li, A. Lee, S. A. Razavi, H. Wu, K. L. Wang, *MRS Bull.* **2018**, *43*, 970.
[11] P. K. Mishra, M. Sravani, A. Bose, S. Bhuktare, *J. Appl. Phys.* **2024**, *135*, 220701.
[12] Y. Shiota, T. Nozaki, F. Bonell, S. Murakami, T. Shinjo, Y. Suzuki, *Nat. Mater.* **2012**, *11*, 39.
[13] W. G. Wang, M. Li, S. Hageman, C. L. Chien, *Nat. Mater.* **2012**, *11*, 64.
[14] C. Song, B. Cui, F. Li, X. Zhou, F. Pan, *Prog. Mater. Sci.* **2017**, *87*, 33.
[15] J.-M. Hu, L.-Q. Chen, C.-W. Nan, *Adv. Mater.* **2016**, *28*, 15.
[16] C. Navarro-Senent, A. Quintana, E. Menéndez, E. Pellicer, J. Sort, *APL Mater.* **2019**, *7*, 030701.
[17] H. Yan, Z. Feng, P. Qin, X. Zhou, H. Guo, X. Wang, H. Chen, X. Zhang, H. Wu, C. Jiang, Z. Liu, *Adv. Mater.* **2020**, *32*, 1905603.
[18] D. Chiba, M. Yamanouchi, F. Matsukura, H. Ohno, *Science* **2003**, *301*, 943.
[19] D. Chiba, M. Sawicki, Y. Nishitani, Y. Nakatani, F. Matsukura, H. Ohno, *Nature* **2008**, *455*, 515.
[20] H. Ohno, D. Chiba, F. Matsukura, T. Omiya, E. Abe, T. Dietl, Y. Ohno, K. Ohtani, *Nature* **2000**, *408*, 944.
[21] M. U. Fayaz, Q. Wang, S. Liang, H. Bai, F. Pan, C. Song, *Acc. Mater. Res.* **2024**, *5*, 648.
[22] Z. Ma, S. Martins, Z. Tan, S. Chen, E. Monteblanco, M. O Liedke, M. Butterling, A. G Attallah, E. Hirschmann, A. Wagner, A. Quintana, E. Pellicer, D. Ravelosona, J. Sort, E. Menéndez, *Adv. Funct. Mater.* **2019**, *34*, 2312827.
[23] A. Molinari, H. Hahn, R. Kruk, *Adv. Mater.* **2019**, *31*, 1806662.
[24] A. J. Tan, M. Huang, C. O. Avci, F. Büttner, M. Mann, W. Hu, C. Mazzoli, S. Wilkins, H. L. Tuller, G. S. D. Beach, *Nat. Mater.* **2019**, *18*, 35.
[25] K-Y Lee, S. Jo, A. J. Tan, M. Huang, D. Choi, J. H. Park, H.-I. Ji, J.-W. Son, J. Chang, G. S. D. Beach, S. Woo, *Nano Lett.* **2020**, *20*, 3435.
[26] P. Monalisha, Z. Ma, E. Pellicer, E. Menéndez, J. Sort, *Adv. Electron. Mater.* **2023**, *9*, 2300249.
[27] P. Monalisha, M. Ameziane, I. Spasojevic, E. Pellicer, R. Mansell, E. Menéndez, S. van Dijken, J. Sort, *Small Sci.* **2024**, *4*, 2400133.
[28] Q. Yang, L. Wang, Z. Zhou, L. Wang, Y. Zhang, S. Zhao, G. Dong, Y. Cheng, T. Min, Z. Hu, W. Chen, K. Xia, M. Liu, *Nat. Commun.* **2018**, *9*, 991.
[29] A. E. Kossak, M. Huang, P. Reddy, D. Wolf, G. S. D. Beach, *Sci. Adv.* **2023**, *9*, eadd0548.
[30] M. Ameziane, R. Rosenkamp, L. Flajšman, S. van Dijken, R. Mansell, *Appl. Phys. Lett.* **2023**, *122*, 232401.
[31] B. X. Tran, J.-H. Ha, W.-C. Choi, S. Yoon, T.-H. Kim, J.-I. Hong, *Appl. Phys. Lett.* **2024**, *124*, 112409.
[32] S. Mangin, D. Ravelosona, J. A. Katine, M. J. Carey, B. D. Terris, E. E. Fullerton, *Nat. Mater.* **2006**, *5*, 210.
[33] F. Gimbert, L. Calmels, S. Andrieu, *Phys. Rev. B* **2011**, *84*, 094432.
[34] H.-S. Song, K.-D. Lee, J.-W. Sohn, S.-H. Yang, S. S. P. Parkin, C.-Y. You, S.-C. Shin, *Appl. Phys. Lett.* **2013**, *102*, 102401.
[35] T. Kato, Y. Matsumoto, S. Kashima, S. Okamoto, N. Kikuchi, S. Iwata, O. Kitakami, S. Tsunashima, *IEEE Trans. Magn.* **2012**, *48*, 3288.

[36] G. H. O. Daalderop, P. J. Kelly, F. J. A. den Broeder, *Phys. Rev. Lett.* **1992**, *68*, 682.
[37] M. Arora, N. R. Lee-Hone, T. Mckinnon, C. Coutts, R. Hübner, B. Heinrich, D. M. Broun, E. Girt, *J. Phys. D: Appl. Phys.* **2017**, *50*, 505003.
[38] S. Girod, M. Gottwald, S. Andrieu, S. Mangin, J. McCord, E. E. Fullerton, J.-M. L. Beaujour, B. J. Krishnatreya, A. D. Kent, *Appl. Phys. Lett.* **2009**, *94*, 262504.
[39] G. Eichinger, *J. Electroanal. Chem. Interf. Electrochem.* **1976**, *74*, 183.
[40] S. Liang, R. Chen, Q. Cui, Y. Zhou, F. Pan, H. Yang, C. Song, *Nano Lett.* **2023**, *23*, 8690.
[41] J. Zhang, H. Xue, Z. Li, Y. Song, J. Zhang, Z. Jiang, Q. Jin, Z. Zhang, *Phys. Rev. Applied* **2023**, *20*, 024063.
[42] G. Wu, S. Chen, Y. Ren, Q. Y. Jin, Z. Zhang, *ACS Appl. Nano Mater.* **2019**, *2*, 5140.
[43] D. A. Gilbert, J. Olamit, R. K. Dumas, B. J. Kirby, A. J. Grutter, B. B. Maranville, E. Arenholz, J. A. Borchers, K. Liu, *Nat. Commun.* **2016**, *7*, 11050.
[44] J. de Rojas, A. Quintana, A. Lopeandía, J. Salguero, B. Muñiz, F. Ibrahim, M. Chshiev, A. Nicolenco, M. O. Liedke, M. Butterling, A. Wagner, V. Sireus, L. Abad, C. J. Jensen, K. Liu, J. Nogués, J. L. Costa-Krämer, E. Menéndez, J. Sort, *Nat. Commun.* **2020**, *11*, 5871.
[45] R. A. Duine, K.-J. Lee, S. S. P. Parkin, M. D. Stiles, *Nat. Phys.* **2018**, *14*, 217.
[46] H. Cai, W. Kang, Y. Wang, L. A. D. B. Naviner, J. Yang, W. Zhao, *Appl. Sci.* **2017**, *7*, 929.
[47] J.-M. Hu, C.-W. Nan, *APL Mater.* **2019**, *7*, 080905.
[48] K. L. Wang, H. Lee, P. K. Amiri, *IEEE Trans. Nanotechnol.* **2015**, *14*, 992.
[49] M. Huang, M. U. Hasan, K. Klyukin, D. Zhang, D. Lyu, P. Gargiani, M. Valvidares, S. Sheffels, A. Churikova, F. Büttner, J. Zehner, L. Caretta, K-Y. Lee, J. Chang, J-P Wang, K. Leistner, B. Yildiz, G. S. D. Beach, *Nat. Nanotechnol.* **2021**, *16*, 981.
[50] Z. Chen, H. Sun, X. Zhou, H. Duan, W. Yan, Y. Yin, X. Li, *J. Materiomics* **2022**, *8*, 1141.
[51] J. Jeong, Y. S. Park, M-G Kang, B-G Park, *Adv. Electron. Mater.* **2024**, *11*, 2400535.
[52] Z. Ma, Z. Tan, A. Quintana, I. Spasojevic, N. López-Pintó, F. Sánchez, I. Fina, J. Herrero-Martín, E. Menéndez, J. Sort, *Appl. Phys. Lett.* **2024**, *124*, 202404.
[53] M. Shirpour, G. Gregori, R. Merkle, J. Maier, *Phys. Chem. Chem. Phys.* **2011**,*13*, 937.
[54] Z. Ma, L. Fuentes-Rodriguez, Z. Tan, E. Pellicer, L. Abad, J. Herrero-Martín, E. Menéndez, N. Casañ-Pastor, J. Sort, *Nat. Commun.* **2023**, *14*, 6486.
[55] J. Zhang, J. Zhou, Z-L. Luo, Y. B. Chen, J. Zhou, W. Lin, M.-H. Lu, S.-T. Zhang, C. Gao, D. Wu, Y.-F. Chen, *Phys. Rev. B* **2020**, *101*, 014422.
[56] T. H. Kim, T. R. Paudel, R. J. Green, K. Song, H.-S. Lee, S.-Y. Choi, J. Irwin, B. Noesges, L. J. Brillson, M. S. Rzchowski, G. A. Sawatzky, E. Y. Tsymbal, C. B. Eom, *Phys. Rev. B* **2020**, *101*, 121105(R).
[57] B. T. Thole, P. Carra, F. Sette, G. van der Laan, *Phys. Rev. Lett.* **1992**, *68*, 1943.
[58] P. Carra, B. T. Thole, M. Altarelli, X. Wang, *Phys. Rev. Lett.* **1993**, *70*, 694.
[59] A. Barla, J. Nicolás, D. Cocco, S. M. Valvidares, J. Herrero-Martín, P. Gargiani, J. Moldes, C. Ruget, E. Pellegrin, S. Ferrer, *J. Synchrotron Radiat.* **2016**, *23*, 1507.